Improving thermodynamic profile retrievals from microwave radiometers by including Radio Acoustic Sounding System (RASS) observations

Irina V. Djalalova[1,2], David D. Turner[3], Laura Bianco[1,2],

James M. Wilczak[2], James Duncan[1,2*], Bianca Adler[1,2] and Daniel Gottas[2]

[1] Cooperative Institute for Research in Environmental Sciences (CIRES), Boulder, CO, USA

[2] National Oceanic and Atmospheric Administration, Physical Sciences Laboratory, Boulder, CO, USA

[3] National Oceanic and Atmospheric Administration, Global Systems Laboratory, Boulder, CO USA

[*]Now at WindESCo, Burlington, MA

Corresponding author address: Irina V. Djalalova (Irina.V.Djalalova@noaa.gov), NOAA/Physical Science Laboratory, 325 Broadway, mail stop: PSD3, Boulder, CO 80305. Tel.: 303-497-6238. Fax: 303-497-6181.

22 **Outline**

23 **Abstract**

24 **1. Introduction**

25 **2. XPIA dataset**

26 **2.1 MWR measurements**

27 **2.2 WPR-RASS measurements**

28 **2.3 BAO data**

29 **2.4 Radiosonde measurements**

30 **3. Physical retrievals**

31 **3.1 Iterative retrieval technique**

32 **3.2 Bias-correction of MWR observations using radiosondes or climatology**

33 **3.3 Analysis of physical retrieval characteristics**

34 **4. Results**

35 **4.1 Statistical analysis of the physical retrievals up to 3 km AGL**

36 **4.2 Statistics for the profiles least close to the climatology**

37 **4.3 Virtual temperature statistics**

38 **5. Conclusions**

39 **Appendix A**

40 **Data availability**

41 **Author contribution**

42 **Acknowledgments**

43 **References**

Abstract

Thermodynamic profiles are often retrieved from the multi-wavelength brightness temperature observations made by microwave radiometers (MWRs) using regression methods (linear, quadratic approaches), artificial intelligence (neural networks), or physical-iterative methods. Regression and neural network methods are tuned to mean conditions derived from a climatological dataset of thermodynamic profiles collected nearby. In contrast, physical-iterative retrievals use a radiative transfer model starting from a climatologically reasonable profile of temperature and water vapor, with the model running iteratively until the derived brightness temperatures match those observed by the MWR within a specified uncertainty.

In this study, a physical-iterative approach is used to retrieve temperature and humidity profiles from data collected during XPIA (eXperimental Planetary boundary layer Instrument Assessment), a field campaign held from March to May 2015 at NOAA's Boulder Atmospheric Observatory (BAO) facility. During the campaign, several passive and active remote sensing instruments as well as in-situ platforms were deployed and evaluated to determine their suitability for the verification and validation of meteorological processes. Among the deployed remote sensing instruments were a multi-channel MWR, as well as two radio acoustic sounding systems (RASS), associated with 915-MHz and 449-MHz wind profiling radars.

In this study the physical-iterative approach is tested with different observational inputs: first using data from surface sensors and the MWR in different configurations, and then including data from the RASS into the retrieval with the MWR data. These temperature retrievals are assessed against co-located radiosonde profiles. Results show that the combination of the MWR and RASS observations in the retrieval allows for a more accurate

characterization of low-level temperature inversions, and that these retrieved temperature profiles match the radiosonde observations better than the temperature profiles retrieved from only the MWR in the layer between the surface and 3 km above ground level (AGL). Specifically, in this layer of the atmosphere, both root mean square errors and standard deviations of the difference between radiosonde and retrievals that combine MWR and RASS are improved by mostly 10-20% compared to the configuration that does not include RASS observations. Pearson correlation coefficients are also improved.

A comparison of the temperature physical retrievals to the manufacturer-provided neural network retrievals is provided in Appendix A.

1. Introduction

Monitoring the state of the atmosphere for process understanding and for model verification and validation requires observations from a variety of instruments, each one having its set of advantages and disadvantages. Using several diverse instruments allows one to monitor different aspects of the atmosphere, while combining them in an optimized synergetic approach can improve the accuracy of the information available on the state of the atmosphere.

During the eXperimental Planetary boundary layer Instrumentation Assessment (XPIA) campaign, a U.S. Department of Energy sponsored experiment held at the Boulder Atmospheric Observatory (BAO) in Spring 2015, several instruments were deployed (Lundquist et al., 2017) with the goal of assessing their capability for measuring atmospheric boundary layer meteorological variables. XPIA investigated novel measurement approaches, and quantified uncertainties associated with these measurement methods. While the main interest of the XPIA campaign was on wind and turbulence, measurements of other important atmospheric variables were also collected, including temperature and humidity. Among the deployed instruments were two identical microwave radiometers (MWRs) and two radio acoustic sounding systems (RASS), as well as radiosondes launches.

MWRs are passive sensors, sensitive to atmospheric temperature, humidity and liquid water path (LWP), that allow for a high temporal observation of the state of the atmosphere, with some advantages and limitations. In order to estimate profiles of temperature and humidity from the observed brightness temperatures (Tb), several methods could be applied such as regressions, neural network retrievals, or physical retrieval methodologies which can

include additional information about the atmospheric state in the retrieval process (e.g., Maahn et al. 2020). Microwave radiative transfer models (e.g., Rosenkranz, 1998; Clough et al. 2005) are commonly used to train statistical retrievals, or as forward models used within physical retrieval methods. Advantages of MWRs include their compact design, the relatively high temporal resolution of the measurements (2-3 minutes), the possibility to observe the vertical structure of both temperature and moisture through the lower part of the troposphere during both clear and cloudy conditions, and their capability to operate in a standalone mode. Disadvantages include limited accuracy in the presence of rain, rather coarse vertical resolution, and the necessity to have a site-specific climatology for retrievals. Other disadvantages include the challenges related to performing accurate calibrations (Küchler et al., 2016, and references within), radio frequency interference (RFI), and the low accuracy on the retrieved LWP especially for values of LWP less than 20 g m^{-2} (Turner 2007).

RASS, in comparison, are active instruments that emit a longitudinal acoustic wave upward, causing a local compression and rarefaction of the ambient air. These density variations are tracked by the Doppler radar associated with the RASS, and the speed of the propagating sound wave is measured. The speed of sound is related to the virtual temperature (Tv) (North et al., 1973), and therefore, RASS are used to remotely measure vertical profiles of virtual temperature in the boundary layer. Being an active instrument, the RASS is in general more accurate than a passive instrument (Bianco et al., 2017), but they also come with their own disadvantages. The main limitations of RASS for temperature measurements are the low temporal resolution (typically a 5-min averaged RASS profile is measured once or twice per hour), their limited altitude coverage, and the noise “pollution” that impacts local communities.

132 Adachi and Hashiguchi (2019) have shown that RASS could use parametric speakers to take
133 advantage of their high directivity and very low side lobes. Nevertheless, the maximum height
134 reached by the RASS is limited by sound attenuation, which is a function of both radar
135 frequency and atmospheric conditions (May and Wilczak, 1993) such as temperature, humidity,
136 and the advection of the propagating sound wave out of the radar's field-of-view. Therefore,
137 data availability is usually limited to the lowest several kilometers, depending on the frequency
138 of the radar. In addition, wintertime coverage is usually lower than that in summer, due to
139 increased attenuation of the acoustic signal in cooler and drier environments.

140 To get a better picture of the state of the temperature and moisture structure of the
141 atmosphere, it makes sense to try to combine the information obtained by both MWR and
142 RASS. Integration of different instruments has been and still is a topic of ongoing scientific
143 interest (Han and Westwater 1995; Stankov et al. 1996; Bianco et al., 2005; Engelbart et al.,
144 2009; Cimini et al., 2020; Turner and Löhnert, 2021, to name some). In this study, the focus is
145 on the combination of the MWR and RASS observations in the retrievals to improve the
146 accuracy of the temperature profiles in the lowest 3 km compared to physical retrieval
147 approaches that do not include the information from RASS measurements. Some studies have
148 used analyses from numerical weather prediction (NWP) models as an additional constraint in
149 these variational retrievals (e.g., Hewison 2007; Cimini et al. 2006, 2011; Martinet et al. 2020);
150 however, we have elected not to include model data in this study because we wanted to
151 evaluate the impact of the RASS profiles on the retrievals from a purely observational
152 perspective.

153 This paper is organized as follows: Section 2 summarizes the experimental dataset;
154 Section 3 introduces the principles of the physical retrieval approaches used to obtain vertical
155 profiles of the desired variables; Section 4 produces statistical analysis of the comparison
156 between the different retrieval approaches and radiosonde measurement; finally, conclusions
157 are presented in Section 5.
158

159 **2. XPIA dataset**

160 The data used in our analysis were collected during the XPIA experiment, held in Spring
161 2015 (March-May) at NOAA's BAO site, in Erie, Colorado (Lat.: 40.0451 N, Lon.: 105.0057 W, El.:
162 1584 m MSL). XPIA was the last experiment conducted at this facility, as after almost 40 years
163 of operations the BAO 300-m tower was demolished at the end of 2016 (Wolfe and Lataitis,
164 2018). XPIA was designed to assess the capability of different remote sensing instruments for
165 quantifying boundary layer structure, and was a preliminary study as many of these same
166 instruments were later deployed, among other campaigns, for the second Wind Forecast
167 Improvement Project WFIP2 (Shaw et al., 2019; Wilczak et al., 2019) which investigated flows in
168 complex terrain for wind energy applications, where they were for example used to study cold
169 air pools (Adler et al., 2021) and gap flow characteristics (Neiman et al., 2019; Banta et al.,
170 2020). The list of the deployed instruments included active and passive remote-sensing devices,
171 and in-situ instruments mounted on the BAO tower. Data collected during XPIA are publicly
172 available at https://a2e.energy.gov/projects/xpia. A detailed description of the XPIA
173 experiment can be found in Lundquist et al. (2017), while a specific look at the accuracy of the
174 instruments used in this study can be found in Bianco et al. (2017).

175

176 **2.1 MWR measurements**

177 Two identical MWRs (Radiometrics MP-3000A) managed by NOAA (MWR-NOAA) and by
178 the University of Colorado (MWR-CU), were deployed next to each other at the visitor center
179 ~600 m south of the BAO tower (see Lundquist et al., 2017 for a detailed map of the study
180 area). Prior to the experiment, both MWRs were thoroughly serviced (sensor cleaning, radome
181 replacement, etc.) and calibrated using an external liquid nitrogen target and an internal
182 ambient target. MWRs are passive devices which record the natural microwave emission in the
183 water vapor and oxygen absorption bands from the atmosphere, providing measurements of
184 the brightness temperatures. Both MWRs have 35-channels spanning a range of frequencies,
185 with 21 channels in the lower (22-30 GHz) K-band frequency band, of which 8 channels were
186 used during XPIA: 22.234, 22.5, 23.034, 23.834, 25, 26.234, 28 and 30 GHz; and 14 channels in
187 the higher (51-59 GHz) V-band frequency band, of which all were used in XPIA: 51.248, 51.76,
188 52.28, 52.804, 53.336, 53.848, 54.4, 54.94, 55.5, 56.02, 56.66, 57.288, 57.964 and 58.8 GHz.
189 Frequencies in the K-band are more sensitive to water vapor and cloud liquid water, while
190 frequencies in the V-band are sensitive to atmospheric temperature due to the absorption of
191 atmospheric oxygen (Cadeddu et al., 2013). V-band frequencies or channels can also be divided
192 in two categories: the opaque channels, 56.66 GHz and higher, that are more informative in the
193 layer of the atmosphere from the surface to ~1 km AGL, and the transparent channels, 51-56
194 GHz, that are more informative above 1 km AGL. Both MWRs observed at the zenith and at 15-
195 and 165-degree elevation angles in the north-south plane (referred to as oblique elevation
196 scans and used as their average hereafter; note zenith views have a 90-degree elevation angle).

197 However, when MWRs are deployed in locations with unobstructed views, oblique scans can be
198 performed down to 5 degrees elevation angles and may provide better temperature profile
199 accuracy in the lowest 0-1 or even 0-2 km AGL layers (Crewell and Löhnert, 2007).

200 In addition, each MWR was provided with a separate surface sensor to measure
201 pressure, temperature, and relative humidity at the installation level that was ~2.5 m AGL.
202 Vertical profiles of temperature (T), water vapor density (WVD), and relative humidity (RH)
203 were retrieved in real-time during XPIA every 2-3 minutes using a neural network (NN)
204 approach provided by the manufacturer of the radiometer (Solheim et al. 1998a, and 1998b;
205 Ware et al., 2003). Although the physical retrieval configurations used in this study do not
206 exactly match the NN retrieval configurations, a comparison of both physical and neural
207 network retrievals to the radiosonde temperature data is presented in Appendix A.

208 Both MWRs nominally operated from 9 March to 7 May 2015, although the MWR-NOAA
209 was unavailable between 5-27 April 2015. For the overlapping dates, temperature profiles
210 retrieved from the two MWRs showed very good agreement with less than 0.5 ^{o}C bias and
211 0.994 correlation (Bianco et al., 2017). For this reason, and because the MWR-CU was available
212 for a longer time period, only the MWR-CU (hereafter simply called MWR) is used.

213

214 **2.2 WPR-RASS measurements**

215 Two NOAA wind profiling radars (WPRs), operating at frequencies of 915-MHz and 449-
216 MHz, were deployed at the visitor center (same location as the MWR) during XPIA. These
217 systems are primarily designed to measure the vertical profile of the horizontal wind vector, but
218 co-located RASS also enable the observation of profiles of virtual temperature in the lower

atmosphere, with different resolutions and height coverages depending on the WPR. Thus, the RASS associated with the 915-MHz WPR (hereafter referred to as RASS 915) measured virtual temperature from 120 to 1618 m with a vertical resolution of 62 m, and the 449 MHz RASS (hereafter referred to as RASS 449) sampled the boundary layer from 217 to 2001 m with a vertical resolution of 105 m. The maximum height reached by the RASS is a function of both radar frequency and atmospheric conditions (May and Wilczak, 1993), and is usually lower for RASS 915 data, as will be shown later in the analysis.

The RASS data were processed using a radio frequency interference (RFI)-removal algorithm (performed on the RASS spectra), a consensus algorithm (Strauch et al. 1984) performed on the moment data using a 60% consensus threshold, a Weber-Wuertz outlier removal algorithm (Weber et al., 1993) performed on the consensus averages, and a RASS range-correction algorithm (Görsdorf and Lehmann, 2000) using an average relative humidity setting of 50% determined from the available observations.

2.3 BAO data

The BAO 300-m tower was built in 1977 to study the planetary boundary layer (Kaimal and Gaynor 1983). During XPIA, measurements were collected at the surface (2 m) and at six higher levels (50, 100, 150, 200, 250 and 300 m AGL). Each tower level was equipped with 2 sonic anemometers on orthogonal booms, and one sensor based on a Sensiron SHT75 solid-state sensor to measure temperature and relative humidity with a time resolution of 1 s, and averaged over five minutes. The more accurate temperature and water vapor observations

240 (Horst et al., 2016) at the BAO tower 2 m AGL level are used in the physical retrieval in place of
241 the less accurate MWR surface sensor.
242
243 **2.4 Radiosonde measurements**
244 Between 9 March and 7 May 2015, while the MWR was operational, radiosondes were
245 launched by the National Center for Atmospheric Research (NCAR) assisted by several students
246 from the University of Colorado over three selected periods, one each in March, April, and May.
247 All radiosondes were Vaisala model RS92. There was a total of 59 launches, mostly four times
248 per day, around 1400, 1800, 2200, and 0200 UTC (0800, 1200, 1600 and 2000 local standard
249 time, LST). The first 35 launches, between 9-19 March, were done from the visitor center, while
250 11 launches between 15-22 April, and 13 launches between 1-4 May, were done from the
251 water tank site, ~1000 meters away from the visitor center (see Lundquist et al., 2017 for a
252 detailed map of the study area). The radiosonde measurements included temperature, dew
253 point temperature, and relative humidity to altitudes usually higher than 10 km AGL, with
254 measurements every few seconds. As a first step, for additional verification, the radiosonde
255 data from the 59 launches taken between 9 March and 4 May 2015 were compared to the BAO
256 tower measurements, up to 300 m AGL. These observed data sets match very well, with a
257 correlation coefficient of 0.99 and a standard deviation of ~0.7 ^{o}C. However, one radiosonde
258 profile showed a large bias (> 5 ^{o}C) against all seven levels of BAO temperature measurements
259 and all available Tv measurements from the RASS 915 (eight measurements up to 600 m AGL)
260 and from the RASS 449 (nine measurements up to 1100 m AGL), therefore this particular
261 radiosonde profile was excluded from the statistical analysis. Moreover, while accurate RASS

data can be collected during rain, MWR data could be potentially deteriorated due to water deposition on the radome. Therefore, six profiles (three for March 13, and one each on May 1, 3 and 4) were eliminated from the statistical evaluation. These restrictions lowered the number of total radiosonde launches used in this study to 52.

3. Physical retrievals

One way to combine the active and passive instruments would be to use the RASS observations up to their maximum available height, and stitch them with the profiles obtained from a physical-iterative method using MWR data. To do this, the moisture contribution to the RASS virtual temperatures could be removed by using either the relative humidity measured by the MWR or by a climatology of the moisture term. However, merging these different profiles could result in artificial jumps at the connecting heights.

Alternatively, a physical retrieval (PR) iterative approach can be used to retrieve vertical profiles of thermodynamic properties from the MWR and RASS observations in a synergistic manner (e.g., Maahn et al 2020; Turner and Löhnert 2021). In this case, an optimal estimation-based physical retrieval is initialized with a climatologically reasonable profile of temperature and water vapor, and is iteratively repeated until the computed brightness temperatures match those observed by the MWR within the uncertainty of the observed brightness temperatures and the RASS virtual temperatures within their uncertainties (Rodgers, 2000; Turner and Löhnert, 2014; Cimini et al. 2018; Maahn et al. 2020).

3.1 Iterative retrieval technique

For this study, the PR uses the *TROPoe* retrieval algorithm (formerly *AERIoe*, Turner and Löhnert 2014; Turner and Blumberg 2019; Turner and Löhnert 2021). This algorithm is able to use radiance data from microwave radiometers, infrared spectrometers, and other observations as input. The microwave radiative transfer model, MonoRTM (Clough et al., 2005), serves as the forward model, which is fully functional for the microwave region and was intensively evaluated previously on MWR measurements (Payne et al. 2008; 2011).

We start with the state vector $\mathbf{X_a} = [\mathbf{T, Q,}\ \mathrm{LWP}]^T$, where superscript T denotes transpose, and vectors and matrices are shown in bold. **T** (K) and **Q** (g kg^{-1}) are temperature and water vapor mixing ratio profiles at 55 vertical levels from the surface up to 17 km, with the distance between the levels increasing geometrically with height. LWP is the liquid water path in (g m^{-2}) that measures the integrated content of liquid water in the entire vertical column above the MWR, and is a scalar. For this study, $\mathbf{X_a}$ has dimensions equal to 111 x 1 (two vectors **T** and **Q** with 55 levels each, and LWP). The retrieval framework of Turner and Blumberg (2019) is used, but only using MWR data (no spectral infrared). Here, we demonstrate the extension of the retrieval to include RASS profiles of **Tv**, and the resulting impact this has on the retrieved temperature profiles and information content.

The observation vector **Y** includes temperature and water vapor mixing ratio measured at the surface in-situ, and spectral **Tb** measured by the MWR. The MonoRTM model **F** is used as the forward model from the current state vector **X**, and is then compared to the observation vector **Y,** iterating until the difference between **F(X)** and **Y** is small within a specified uncertainty (Eq 1).

$$\boldsymbol{X_{n+1} = X_n + (S_a^{-1} + K^T S_\varepsilon^{-1} K)^{-1} K^T S_\varepsilon^{-1} [Y - F(X_n) + K(X_n - X_a)]} \quad (1)$$

307 with

308 $$X_a = \begin{bmatrix} \boldsymbol{T} \\ \boldsymbol{Q} \\ LWP \end{bmatrix} \qquad S_a = \begin{bmatrix} \boldsymbol{\sigma_{TT}^2} & \boldsymbol{\sigma_{TQ}^2} & 0 \\ \boldsymbol{\sigma_{QT}^2} & \boldsymbol{\sigma_{QQ}^2} & 0 \\ 0 & 0 & \sigma_{LWP}^2 \end{bmatrix} \qquad \boldsymbol{K_{ij} = \partial F_i / \partial X_j}$$

309 where i and j in the $\mathbf{K}_{ij}$ definition mark channel and vertical level, respectively. The superscripts

310 T and -1 in (1) indicate the transpose and inverse matrix, respectively. The observation vector **Y**

311 and the covariance matrix of the observed data, $\mathbf{S}_\varepsilon$, depending on the configuration used, are

312 equal to:

313 $$Y_1 = \begin{bmatrix} T_{sfc} \\ Q_{sfc} \\ \boldsymbol{Tb_{zenith}} \end{bmatrix} \qquad S_{\varepsilon_1} = \begin{bmatrix} \sigma_{Tsfc}^2 & 0 & 0 \\ 0 & \sigma_{Qsfc}^2 & 0 \\ 0 & 0 & \boldsymbol{\sigma_{Tb_{zenith}}^2} \end{bmatrix}$$

314 $$Y_2 = \begin{bmatrix} T_{sfc} \\ Q_{sfc} \\ \boldsymbol{Tb_{zenith+oblique}} \end{bmatrix} \qquad S_{\varepsilon_2} = \begin{bmatrix} \sigma_{Tsfc}^2 & 0 & 0 \\ 0 & \sigma_{Qsfc}^2 & 0 \\ 0 & 0 & \boldsymbol{\sigma_{Tb_{zenith+oblique}}^2} \end{bmatrix}$$

315 $$Y_3 = \begin{bmatrix} T_{sfc} \\ Q_{sfc} \\ \boldsymbol{Tb_{zenith+oblique}} \\ \boldsymbol{Tv_{RASS915}} \end{bmatrix} \qquad S_{\varepsilon_3} = \begin{bmatrix} \sigma_{Tsfc}^2 & 0 & 0 & 0 \\ 0 & \sigma_{Qsfc}^2 & 0 & 0 \\ 0 & 0 & \boldsymbol{\sigma_{Tb_{zenith+oblique}}^2} & 0 \\ 0 & 0 & 0 & \boldsymbol{\sigma_{Tv_{RASS915}}^2} \end{bmatrix}$$

316 $$Y_4 = \begin{bmatrix} T_{sfc} \\ Q_{sfc} \\ \boldsymbol{Tb_{zenith+oblique}} \\ \boldsymbol{Tv_{RASS449}} \end{bmatrix} \qquad S_{\varepsilon_4} = \begin{bmatrix} \sigma_{Tsfc}^2 & 0 & 0 & 0 \\ 0 & \sigma_{Qsfc}^2 & 0 & 0 \\ 0 & 0 & \boldsymbol{\sigma_{Tb_{zenith+oblique}}^2} & 0 \\ 0 & 0 & 0 & \boldsymbol{\sigma_{Tv_{RASS449}}^2} \end{bmatrix}$$

317 Note that the 2-m surface-level observations of temperature and water vapor mixing
318 ratio (T_{sfc} and Q_{sfc}, respectively) are included as part of the observation vector **Y**, and thus the
319 uncertainties (0.5 K for temperature and less than 0.4 g kg^{-1} for mixing ratio) in these
320 observations are included in $\mathbf{S_\varepsilon}$.
321 The mean state vector of the climatological estimates, or a "prior" vector $\mathbf{X_a}$, is a key
322 component in the optimal estimation framework and it is the first guess of the state vector **X**,
323 $\mathbf{X_1}$ in Eq. (1). It provides a constraint on the ill-posed inversion problem. The prior is calculated
324 independently for each month of the year from climatological sounding profiles (using 10 years
325 of data) in the Denver area. **T**he covariance matrix, $\mathbf{S_a}$, of the "prior" vector includes not only
326 temperature or water vapor variances but also the covariances between them. Using around
327 3,000 radiosondes launched by the NWS in Denver, each radiosonde profile is interpolated to
328 the vertical levels used in the retrieval, after which the covariance of temperature and
329 temperature, temperature and humidity, and humidity and humidity is computed for different
330 levels. LWP is arbitrarily assigned in $\mathbf{X_a}$, with large values chosen for its uncertainty in $\mathbf{S_a}$, so that
331 it does not impact (constrain) the retrieval.
332 Four configurations are chosen for the observational vector **Y** ($\mathbf{Y_1}$, $\mathbf{Y_2}$, $\mathbf{Y_3}$, and $\mathbf{Y_4}$). In each
333 of these, the surface observations are obtained by the 2-m BAO *in-situ* measurements of
334 temperature and humidity. The MWR provides **Tb** measurements from 22 channels from the
335 zenith scan for the zenith only configuration ($\mathbf{Y_1}$), while when using the zenith plus oblique Tb
336 inputs ($\mathbf{Y_2}$, $\mathbf{Y_3}$, and $\mathbf{Y_4}$) the same 22 channels were used from the zenith scans together with only
337 the four opaque channels (56.66, 57.288, 57.964 and 58.8 GHz) from the oblique scans. Using
338 additional measurements from the co-located radar systems with RASS, the observational

339 vector is further expanded with either RASS 915 ($\mathbf{Y_3}$) or RASS 449 ($\mathbf{Y_4}$) virtual temperature

340 observations. The covariance matrix of the observed data, $\mathbf{S_\epsilon}$, depends on the chosen $\mathbf{Y_i}$ as seen

341 in the matrix $\mathbf{S_{\epsilon i}}$ (with i = 1:4) descriptions, with increasing dimensions from $\mathbf{Y_1}$ to $\mathbf{Y_2}$ and

342 additional increasing dimensions to $\mathbf{Y_3}$ or $\mathbf{Y_4}$ through the multi-level measurements of the RASS

343 (Turner and Blumberg, 2019). Table 1 summarizes the observational information included in

344 these four different configurations of the PR.

345

	T_{sfc}	Q_{sfc}	Tb_{zenith}	$Tb_{oblique}$	$Tv_{RASS915}$	$Tv_{RASS449}$
$\mathbf{Y_1}$ = *MWRz*	*X*	*X*	*X*			
$\mathbf{Y_2}$ = *MWRzo*	*X*	*X*	*X*	*X*		
$\mathbf{Y_3}$ = *MWRzo915*	*X*	*X*	*X*	*X*	*X*	
$\mathbf{Y_4}$ = *MWRzo449*	*X*	*X*	*X*	*X*		*X*

346 *Table 1. Four PR configurations corresponding to the four observational $\mathbf{Y_i}$ vectors in Eq. (1).*

347

348 The uncertainty in the MWR Tb observations was set to the standard deviation from a

349 detrended time-series analysis for each channel during cloud-free periods. The method to

350 detect those cloud-free periods is described in detail in Section 3.2. The derived uncertainties

351 ranged from 0.3 K to 0.4 K in the 22 to 30 GHz channels, and 0.4 to 0.8 K in the 52 to 60 GHz

channels. We assumed that there was no correlated error between the different MWR channels.

For the RASS, co-located RASS and radiosonde profiles were compared and the standard deviation of the differences in Tv were determined as a function of the radar's signal-to-noise ratio (SNR). This relationship resulted in uncertainties that ranged from 0.8 K at high SNR values to 1.5 K at low SNR values. Again, we assumed that there was no correlated error between different RASS heights. Following these assumptions, the covariance matrix $\mathbf{S_\varepsilon}$ is diagonal.

The Jacobian matrix, **K**, is computed using finite differences by perturbing the elements of **X** and rerunning the forward model. It has dimensions m x 111, where m is the length of the vector $\mathbf{Y_i}$, therefore its dimension increases correspondingly with the inclusion of more observational data. **K** makes the "connection" between the state vector and the observational data and should be calculated at every iteration.

3.2 Bias-correction of MWR observations using radiosondes or climatology

Observational errors propagate through retrieval into the derived profiles (i.e. the bias of the observed data will contribute to a bias in the retrievals). For that, retrieval uncertainties in Eq. (1) from $\mathbf{Y} = \mathbf{Y_1}$ or $\mathbf{Y_2}$ derive only from uncertainties in surface and MWR data, while retrieval uncertainties from $\mathbf{Y} = \mathbf{Y_3}$ or $\mathbf{Y_4}$ come from uncertainties in the surface, MWR, and RASS measurements.

The bias of the retrieval depends on both the absolute accuracy of the forward model and on any observational systematic offset, of which the systematic error in the MWR observations could potentially be reduced through application of an MWR Tb bias-correction

374 procedure. In this study, two different approaches were used for the bias-correction: the first is
375 based on a comparison to the radiosondes, while the second uses climatological profiles. The
376 first method could be used for a field campaign where occasional co-located radiosonde
377 launches are taken, while the second would be used for deployments without any supporting
378 radiosonde observations.

379 For both approaches, the first step is to identify clear-sky periods during which the bias
380 can be estimated (to eliminate uncertainties associated with clouds) and subsequently the bias
381 can be removed from the observed MWR Tbs. One method to identify clear-sky times is to use
382 a time-series of Tb observations in the 30 GHz liquid water sensitive channel of the MWR.

383 The standard deviation of the MWR Tb in the 30 GHz channel is calculated over a time
384 frame of one hour centered at the radiosonde launch time. The data from the zenith scan and
385 the averaged oblique scans are reviewed separately. Liquid-cloud free periods were identified
386 by cases where the temporal standard deviation was small (< 0.4 K), and more than 35
387 radiosonde profiles were classified as being launched in clear skies. The usage of the standard
388 deviation from the time-series from the oblique scans, with the same 0.4 K restriction, reduces
389 the number of the clear-sky radiosonde profiles to 18. For those chosen 18 radiosonde profiles,
390 the Tb is calculated from radiosonde temperature profiles through MonoRTM at each of the
391 MWR channels. The mean difference between these calculated radiosonde Tbs and measured
392 MWR Tbs forms the Tb bias with which the MWR Tb data can be corrected. This bias-correction
393 method will be referred to as 'radiosonde BC'.

394 While this radiosonde BC method can be employed for the XPIA dataset, for other
395 campaigns this approach would not be possible if co-located radiosonde observations were not

396 available. For this situation, an alternative method for correcting the MWR Tb biases is
397 presented. There are often spectral features in the observed minus computed brightness
398 temperature residuals that could not be explained by any physically realistic atmospheric
399 profiles, and can only result because of a calibration error in the observations. This alternative
400 bias-correction method is aimed purely to remove this unphysical spectral signature. In this
401 method, to choose clear-sky periods, the 30 GHz channel MWR Tb data are used on a daily
402 basis. The standard deviation of the MWR Tb is calculated as the average of standard deviations
403 in a one-hour sliding window through all data points of a day. Four clear-sky days were
404 identified using a threshold of 0.4 K on the standard deviation: March 10 and 30, and April 13
405 and 29, 2015. The Tb bias is then computed for each of the 22 channels as the averaged
406 difference between the observed Tb from the MWR zenith observations and the forward model
407 calculated Tbs at zenith using the TROPoe-retrieved profiles ($\mathbf{Y_1}$) of those selected clear-sky
408 days. This method identified spectral calibration errors in the MWR observations that could not
409 be explained by physically realistic atmospheric profiles. This bias-correction technique, which
410 accounts for those unphysical spectral calibration features, will be referred to as 'TROPoe BC'.
411 Fig. 1 shows the Tb biases found for all 22 MWR channels from both bias-correction
412 approaches. The biases calculated with the radiosonde BC scheme are shown for all channels
413 used in our analysis: 22 channels of the zenith scan, in red, and four V-band opaque channels of
414 the oblique scans, in blue. The black and green triangles represent the biases calculated using
415 the TROPoe BC approach for zenith and for zenith+oblique scans, respectively. All biases are
416 presented with associated uncertainties (error bars representing the standard deviation over all

radiosondes for radiosonde BC, and mean observation Tb vector uncertainties for chosen four clear-sky days for TROPoe BC).

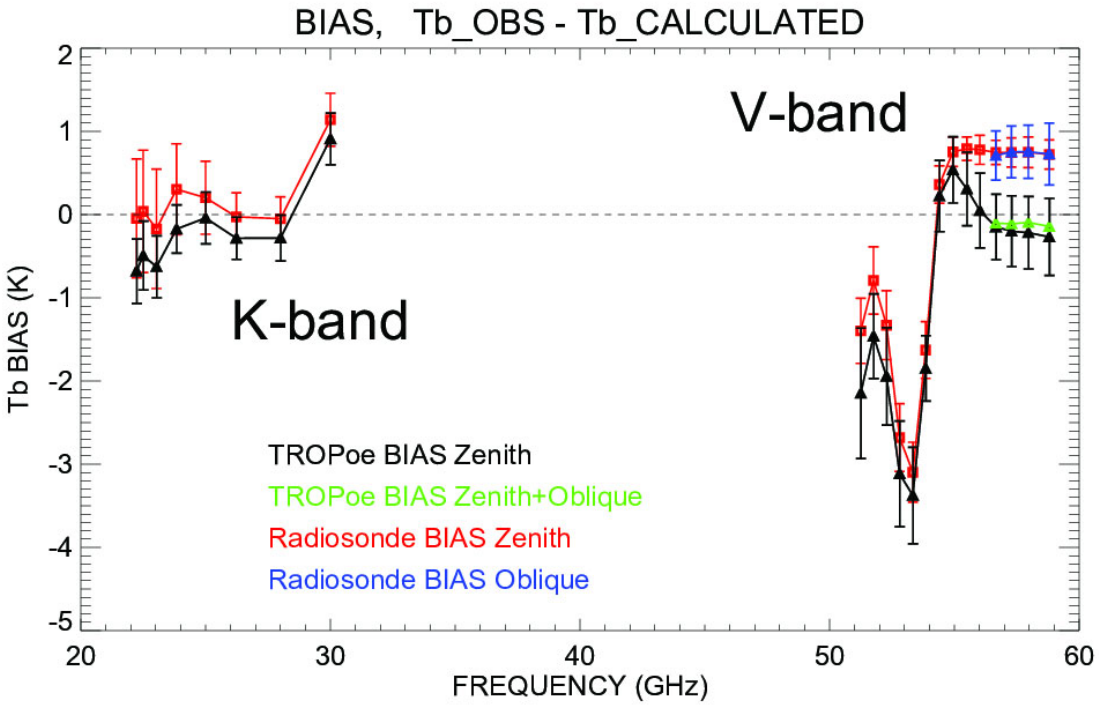

Fig. 1. Tb biases derived from the radiosonde BC method (and TROPoe BC method) in all 22 MWR channels of the zenith scan in red (and in black), and in the four opaque channels of the oblique scans in blue (and in green).

The biases from the two bias-correction schemes are within the uncertainties of each other for most of the channels except at the higher frequencies in the V-band. Biases in the most opaque channels are significantly affected by the accuracy of the boundary layer temperature profiles. When TROPoe BC is used, a monthly average prior temperature profile is used in the PR, and thus differences between this prior profile and the actual temperature

428 profile can result in a spectral bias in the more opaque MWR channels. On the contrary, the
429 radiosonde BC uses a direct measurement of the temperature profile (from the radiosonde),
430 and thus is more accurate. It is also important to note that, in both approaches, the biases in
431 the opaque channels for zenith and for oblique scans (for radiosonde BC these are red and blue,
432 respectively; and for the TROPoe BC these are black and green, respectively) are very similar to
433 each other. This supports the assumption that the true bias is nearly independent of the scene,
434 or that the sensitivity to the scene (e.g., zenith or off-zenith) is small.

435 The bias-correction methods were applied by removing the corresponding calculated
436 biases from the MWR Tb observations before the retrievals were performed. Later in Section 4,
437 differences in the retrieved temperature profiles will be shown when using the two bias-
438 correction approaches. These differences will be more evident in the temperature profiles
439 exhibiting near-ground temperature inversions.

440 However, the final goal of this study is not to assess the sensitivity to different bias-
441 correction approaches but to verify that the inclusion of RASS observations does improve
442 retrieved temperature profiles, independently of the bias-correction method used.

443

444 **3.3 Analysis of physical retrieval characteristics**

445 The retrieved profiles of the four different PR configurations presented in Table 1
446 (MWRz, MWRzo, MWRzo915, MWRzo449) were compared to the radiosonde profiles. To
447 compare radiosonde observations against the PR profiles, all radiosonde profiles were
448 interpolated vertically to the same PR heights, and PR profiles were averaged in the time
449 window between 15 minutes before and 15 minutes after each radiosonde launch. Since the

radiosonde ascends quite quickly in the lowest kilometers of the atmosphere (~15-20 min to reach 5 km), the 30-minute temporal window is estimated to be representative of the same volume of the atmosphere measured by the radiosonde. BAO tower temperature and mixing ratio data at the seven available levels were used as an additional validation dataset, without any vertical interpolation, averaged in the time window between 15 minutes before and 15 minutes after each radiosonde launch.

As an example of the different temperature retrievals and their relative performance, data obtained on 17 March 2015 at 2200 UTC are presented in Fig. 2. Temperature profiles up to 2 km AGL retrieved from the four PR configurations (MWRz, MWRzo, MWRzo915, MWRzo449, using the radiosonde BC) are compared to the radiosonde data in red and to the BAO measurements in blue squares. Note that all four of the PRs match the BAO observations reasonably well near the ground. The MWRz and MWRzo profiles are very smooth and depart quite substantially from the radiosonde measurements, being unable to reproduce the more detailed structure of the atmospheric temperature profile measured by the radiosonde, while the MWRzo449 profile (in light-blue) demonstrates a better agreement with both the radiosonde and BAO measurements (blue squares). The MWRzo915 profile (in purple) also tries to follow the elevated temperature inversion observed by the radiosonde, successfully only in the lower part of the atmosphere (below 1 km AGL) where RASS 915 measurements are available. This behavior will be also addressed in the following section and in the statistical analysis presented later in the manuscript.

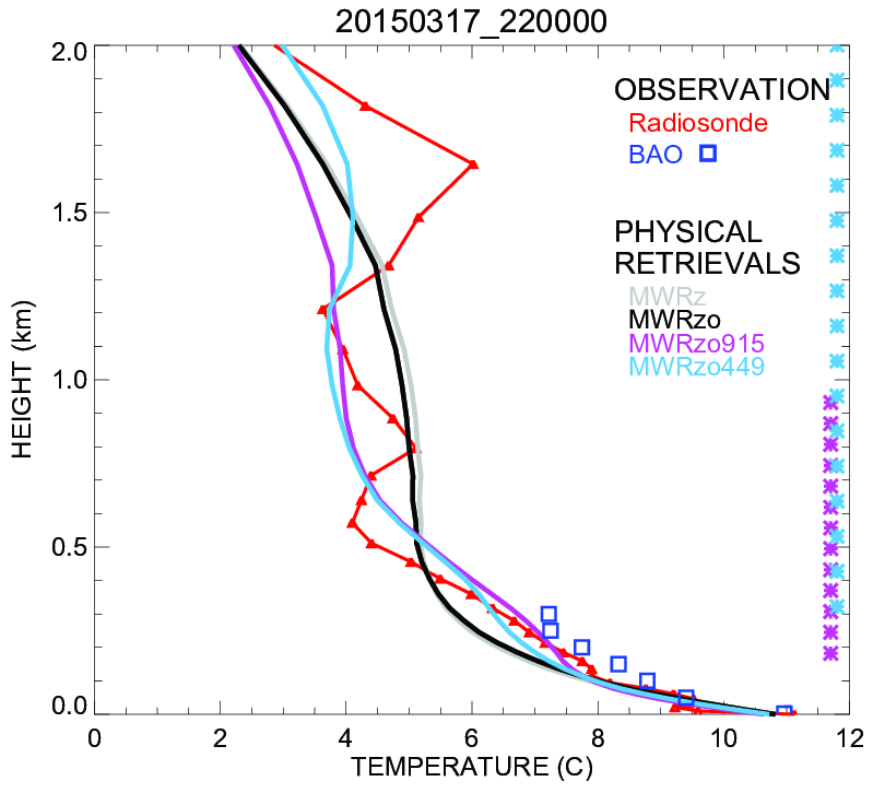

Fig. 2. Temperature profiles obtained by the four PR configurations, after applying the radiosonde BC on the MWR Tbs: MWRz in gray, MWRzo in black, MWRzo915 in purple, and MWRzo449 in light-blue. These retrievals are compared to radiosonde measurements, in red, and BAO tower observations, in blue squares. The heights with available RASS virtual temperature measurements (RASS 915 in purple and RASS 449 in light-blue) are marked by the asterisks on the right Y-axis.

An asset of TROPoe is that several characteristics of the PRs can be obtained from two matrices, the averaging kernel, **Akernel,** and the posterior covariance matrix, **Sop** (Masiello et al., 2012; Turner and Löhnert, 2014, Turner and Bloomberg, 2019), calculated as:

$$\boldsymbol{Akernel = B^{-1}\, K^{T}\, S_{\varepsilon}^{-1}\, K} \quad (2)$$

and:

$$\boldsymbol{Sop = B^{-1}} \quad (3)$$

where:

$$\boldsymbol{B = S_a^{-1} + K^{T}\, S_{\varepsilon}^{-1}\, K}$$

All matrices, **Akernel**, **Sop**, and **B**, have dimensions 111 x 111 in our configuration. While the top left corner of the **Akernel** matrix (1:55, 1:55) is devoted to temperature, called further in the text **ATkernel**, the next (56:110, 56:110) elements are devoted to the water vapor mixing ratio, called **AQkernel**.

The **Akernel** provides useful information about the calculated retrievals, such as vertical resolution and degrees of freedom for signal at each level. The rows of the **Akernel** provide the smoothing functions (Rodgers, 2000) that could be applied to the radiosonde profiles (Eq. 4) to minimize the vertical representativeness error in the comparison between the various retrievals and the radiosonde profiles due to very different vertical resolutions of these profiles (Turner and Löhnert, 2014).

Smoothed radiosonde observed profiles can be computed using the averaging kernel, as:

$$\boldsymbol{X_{smoothed\_radiosonde} = Akernel\ (X_{radiosonde} - X_a) + X_a} \quad (4)$$

The **Akernel** in Eq. (2) depends on the retrieval parameters (e.g., which datasets are used in the **Y** vector, the values assumed in the observation covariance matrix $\mathbf{S_\varepsilon}$, and the

sensitivity of the forward model), so for our four PR configurations it is possible to calculate four different kernels from Eq. (2).

For each of the four **Akernel**s, a smoothed radiosonde profile can be computed for each radiosonde profile using Eq. (4). In the presence of temperature inversions or other particular structures in the atmosphere, these smoothed profiles can be quite different from each other and also from the original unsmoothed radiosonde profile. Consequently, while comparison of the retrievals to the relative Akernel-smoothed radiosonde profiles can be used to minimize the vertical representativeness effects due to the different vertical resolutions of these profiles, we note that a statistical comparison between the four configurations of the observational vector would not be fair if each of their retrieved profiles is compared to a different Akernel-smoothed radiosonde profile. Therefore, in the statistical analysis presented later in the manuscript (section 4.2), mean bias, root mean square error (RMSE), and Pearson correlation coefficients will be computed between the various TROPoe retrieval configurations and the unsmoothed radiosonde profiles, just interpolated to the same vertical levels of the retrieved profiles.

The **ATkernel** can help understand the differences in the retrieved temperature profiles obtained by the configurations using additional RASS data, shown in the example of Fig. 2. Figure 3a includes the temperature profiles of the radiosonde (unsmoothed and **ATkernel**'s smoothed) and PRs of MWRzo and MWRzo449 for the same example as in Fig. 2. Due to the inclusion of RASS measurements, the **ATkernel**-smoothed radiosonde profile of the MWRzo449 configuration (dashed light-blue line) is closer to the original radiosonde data (in red) compared to the black dashed profile of the MWRzo's **ATkernel**-smoothed radiosonde profile. Additionally, the rows of the **ATkernel** provide a measure of the retrieval smoothing as a

526 function of altitude, so the full-width half maximum (FWHM) of each **ATkernel** row estimates
527 the vertical resolution of the retrieved solution at each vertical level (Maddy and Barnet, 2008;
528 Merrelli and Turner, 2012). Plots of this vertical resolution as a function of the height for the
529 MWRzo PR and for the MWRzo449 PR are included in Fig. 3b. This plot shows that the
530 additional observations from the RASS 449 significantly improve the vertical resolution of the
531 retrievals.

532 The posterior covariance matrix, **Sop,** provides a measure of the uncertainty of the
533 retrievals while the square root of the diagonal of this matrix is used to specify the 1-σ errors in
534 the profiles of temperature or mixing ratio. Also, **Sop** shows the level-to-level dependency of
535 the retrievals, and in an ideal case should have all non-diagonal elements equal to zero.
536 Converted to a correlation matrix, it is possible to visualize these dependencies, as presented in
537 Fig. 3c, d. The use of additional RASS data (MWRzo449 **Sop**, Fig. 3d) reduces the off-diagonal
538 covariances, therefore substantially decreasing the correlations in those areas compared to the
539 MWRzo **Sop** (Fig. 3c).

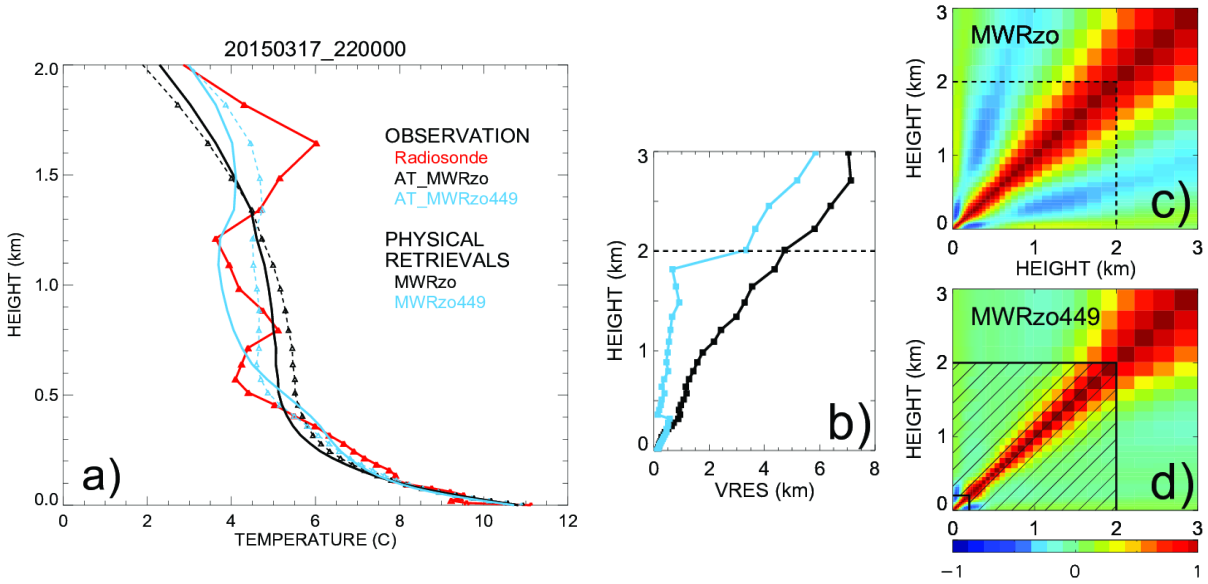

540

*Fig. 3. a) observed temperature profiles from radiosonde, in red, from **ATkernel**s smoothed radiosonde, **AT_MWRzo** in dashed black, and **AT_MWRzo449** in dashed light-blue; PRs from MWRzo PR in solid black, and from MWRzo449 PR in solid light-blue. b) vertical resolution (VRES) as a function of the height for the MWRzo PR (black), and for the MWRzo449 PR (light-blue). c) and d) 3 x 3 km (37 x 37 levels) **Sop** matrices, converted to correlation matrices, for the MWRzo PR (c), and for the MWRzo449 PR (d). Dashed lines on plots b)-d) mark 2 km AGL. Hatched area on panel d marks the RASS measurement heights.*

To understand the level-to-level correlations among the 4 different retrieval configurations in Table 1, the **Sop** matrices were averaged over all radiosonde events, and converted to correlation matrices (Fig. 4). A clearly visible narrowing of the spread around the main diagonal and correlation reduction in the off-diagonal elements result by adding additional observations, from MWR zenith only (Fig. 4a), to MWR zenith-oblique (Fig. 4b), to the larger impact obtained by the usage of the RASS 915 (Fig. 4c), concluding with the RASS 449 (Fig. 4d) data. The mean retrieval uncertainty profile for each of the PR configurations is presented in Fig. 4e. The uncertainty of the MWRzo449 retrieval up to 1 km AGL is around 0.5 ^{o}C while the other retrievals have higher uncertainties of up to 1 ^{o}C. The higher accuracy of the MWRzo449 retrievals is because that configuration has more observational information compared to the other retrieval configurations.

Other statistically important features to analyze in the PRs, besides their uncertainty, are the vertical resolution already introduced in the example of Fig. 3b, and the degree of freedom for signal (DFS). These two features, derived from the **Akernel**s of each PR

563 configuration, averaged over all radiosonde events, are shown in Fig 4f and 4g. The vertical
564 resolution (Fig. 4f) shows the width of the atmosphere layer used for each retrieval height,
565 computed as the full-width half-maximum value of the averaging kernel. The cumulative DFS
566 profile (Fig. 4g) is a measure of the number of independent pieces of information in the
567 observations below the specified height. For example, at the 1 km AGL level the vertical
568 resolution of MWRzo449 is 0.5 km (i.e. information is from +/- 0.5 km around the retrieval
569 height is considered in the retrieval), while all other retrievals use the information from more
570 than +/- 1.5 km. Also, the DFS, as a cumulative measure, shows an increase in pieces of
571 information from MWRz to MWRzo for the whole profile and from MWRzo to MWRzo915 and
572 to MWRzo449 above ~0.2 km where RASS data are available. The DFS of MWRzo915 is higher
573 compared to the DFS of MWRzo449 in the 0.2-0.5 km AGL layer because RASS 915 data have
574 denser measurements there. It is also important to note that there is no additional information
575 added to any of the retrievals above 2km AGL, i.e. the slope of the cumulative DFS profiles are
576 equal. Despite that, the statistical analysis of the PRs up to 3 km AGL, shown in Section 4, will
577 prove that the retrieval improvements obtained by including the RASS are found even above
578 the height of the RASS measurements availability.
579

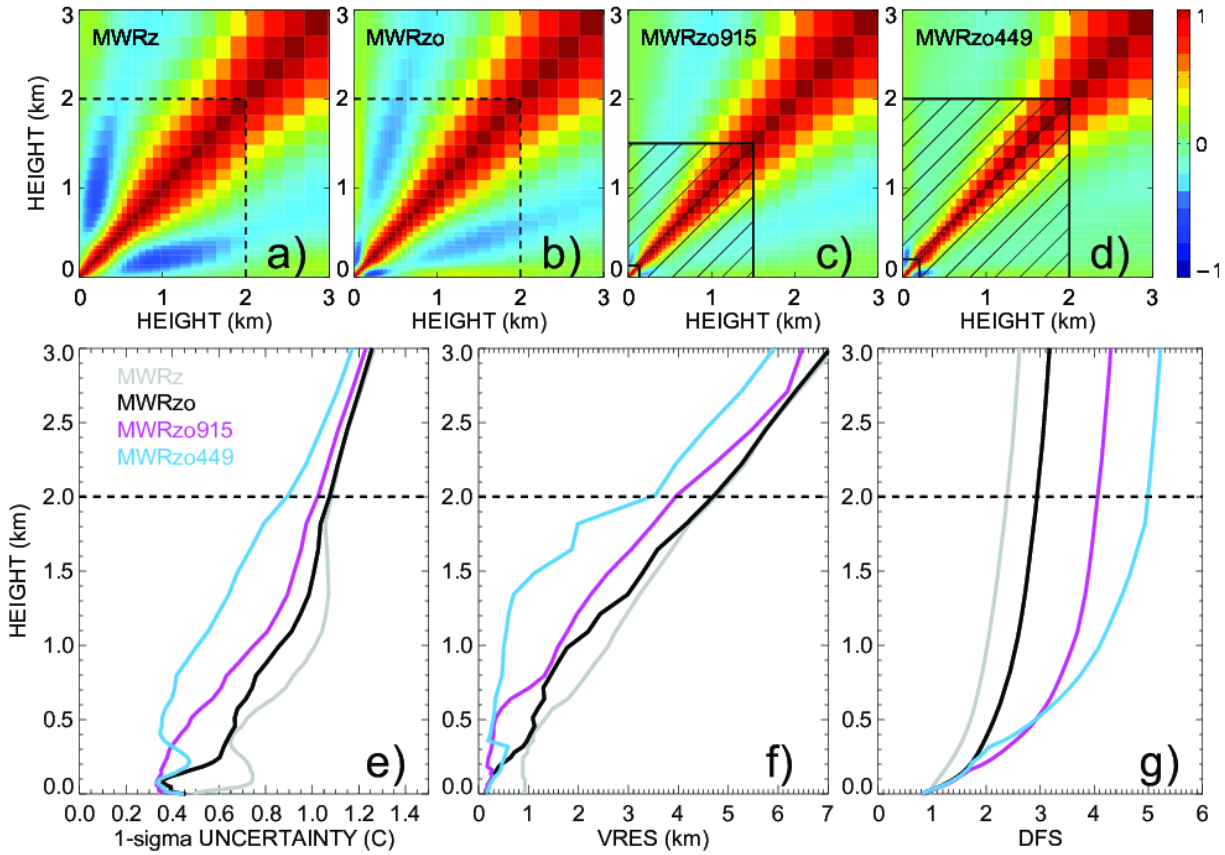

580

581 *Fig. 4. Top row: The mean **Sop**s, displayed as correlation matrices, for (a) MWRz, (b) MWRzo, (c)*

582 *MWRzo915, and (d) MWRzo449, averaged over all radiosonde events. Hatched area on panels*

583 *c) and d) marks the RASS maximum measurement heights. Bottom panels: (e) one-sigma*

584 *uncertainty derived from the posterior covariance matrix in ^{o}C, (f) vertical resolution (VRES) in*

585 *km, and (g) cumulative Degree of Freedom (DFS) as a function of height for temperature,*

586 *averaged over all radiosonde events (MWRz is in gray, MWRzo is in black, MWRzo915 is in*

587 *purple, and MWRzo449 is in light-blue). Dashed lines mark 2 km AGL on all panels.*

588

589 The improvements from MWRz (in gray) to MWRzo (in black), to MWRzo915 (in purple),

590 and finally to MWRzo449 (in light-blue) are visible in all three panels (Fig 4e-g), whereas

591 MWRzo449 has the lowest 1-σ uncertainty and highest DFS compared to the other PRs,
592 particularly below 2 km AGL, where RASS 449 measurements are available. Finally, it is
593 interesting that below 200 m AGL the MWRzo915 has slightly smaller lowest 1-σ uncertainty
594 and vertical resolution relative to the MWRzo449, as could be expected due to the first
595 available height of the RASS 915 being lower (120 m AGL) than the first available height for the
596 RASS 449 (217 m AGL) and due to the finer vertical resolution of the 915-MHz RASS. This
597 suggests that if additional observations were available in the lowest several 100 m of the
598 atmosphere where RASS measurements are not available, improvements might be even better
599 closer to the surface, where temperature inversions, if present, are sometimes difficult to
600 retrieve correctly.
601

602 **4. Results**

603 **4.1 Statistical analysis of physical retrievals up to 3km AGL**

604 Several cases were found during XPIA when the temperature profile exhibited
605 inversions, with the lowest happening in the surface layer. Figure 5 shows one of the most
606 complex cases, with several temperature inversions visible in the temperature profile from the
607 radiosonde (red line), in the temperature measurements from the BAO tower (blue squares),
608 and in the virtual temperature measured by the RASS 449 (light blue triangles). Note that the
609 virtual temperature profile is in close agreement with the temperature measured by
610 radiosonde.

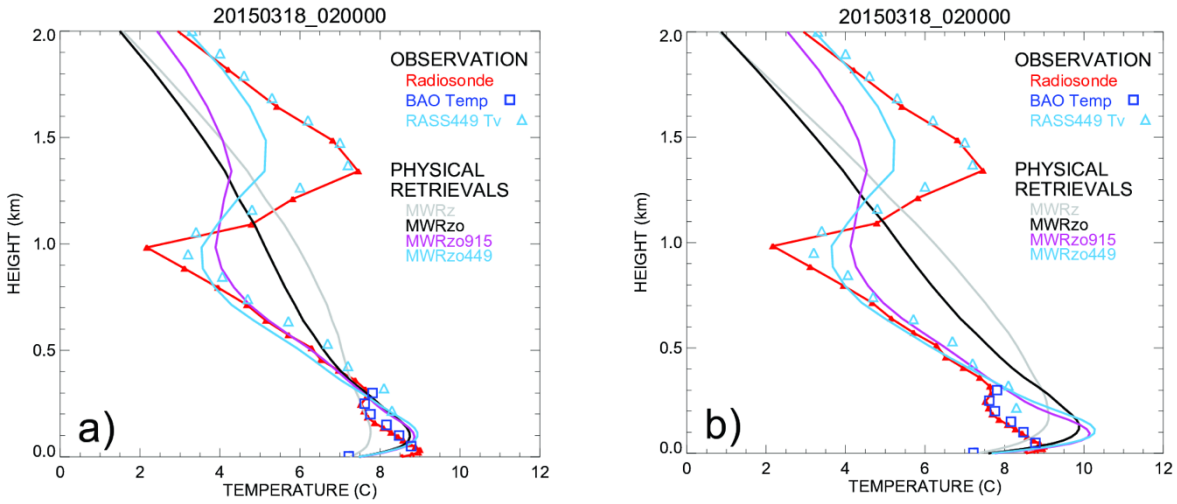

611

612 *Fig. 5. As in Fig. 2 but for 18 March 2015 at 0200 UTC. The RASS 449 virtual temperature is*
613 *included as light blue triangles. a) shows the PRs obtained after applying the radiosonde BC, and*
614 *b) shows the PRs obtained after applying the TROPoe BC on the MWR Tbs.*

615

616 Figure 5 also illustrates the difference in the temperature profiles, especially between 0-
617 300m AGL, for the two different bias-correction schemes, which show noticeable differences in
618 the biases of the opaque channels (especially important for the near-ground retrievals)
619 presented in Fig. 1. As expected, the radiosonde BC method yielded a retrieved profile closer to
620 the radiosonde temperature profile than when using TROPoe BC, for which the inversion in the
621 temperature profile close to the surface is too accentuated (particularly the black, purple, and
622 cyan lines, all of which used oblique scan data).

623 The relative statistical behavior (Pearson correlation, RMSE, and bias) of the PRs for
624 both temperature and mixing ratio against radiosondes is shown in Figure 6, using both bias-
625 correction approaches. PRs obtained after applying the radiosonde BC (Fig. 6a) present overall

smaller RMSE and bias (the latter almost equal to zero up to 3 km AGL) and slightly higher correlations compared to the statistics of the PRs obtained after applying the TROPoe BC (Fig. 6b). This could be expected since for the comparison in Fig. 6a a subset of the radiosondes was already used for the Tb bias correction. Also, the different retrievals show a narrower distribution for the panels in Fig. 6a. Nevertheless, the results obtained when applying either bias-correction methods (in Fig. 6a, b) consistently show the improvement obtained when the RASS observations are used, with relatively smaller bias and RMSE in the 3 km layer AGL. The correlation is mainly improved above 1 km, when RASS observations are included.

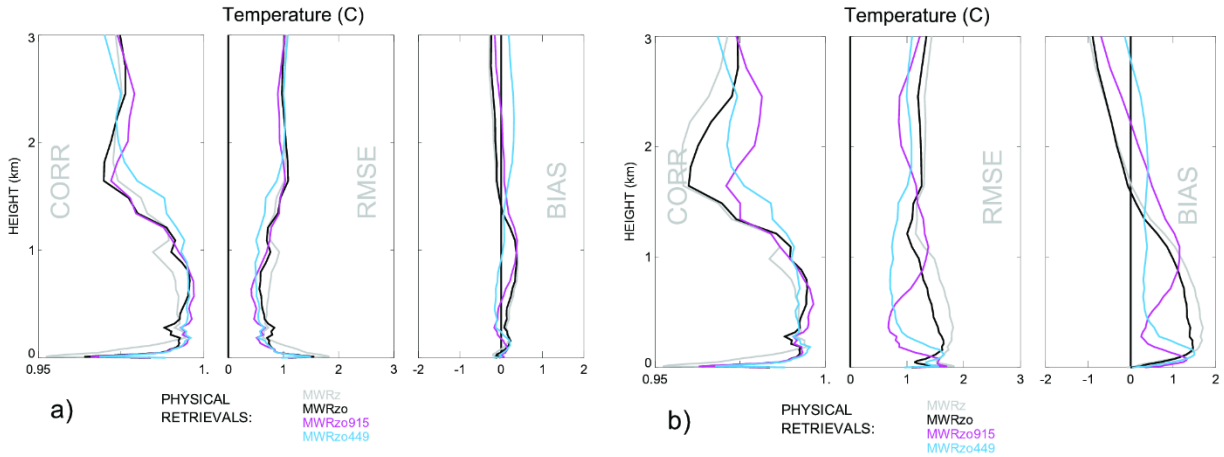

Fig. 6. Pearson correlation, RMSE, and mean bias for temperature profiles of MWRz in gray, MWRzo in black, MWRzo915 in purple, and MWRzo449 in light-blue for the radiosonde BC bias-correction method in a) and TROPoe BC method in b).

Besides temperature profiles, the PRs also provide water vapor mixing ratio profiles. It is understandable that the different configurations of PRs are not noticeably different from each other in relation to moisture, because the Tv observations from the RASS are dominated by the ambient temperature (not moisture), and thus have little impact on the water vapor retrievals.

642 We found that the **AQKernel**s are almost identical for all four PR configurations (not shown).
643 Detailed statistical evaluation of the PRs mixing ratio profiles are presented in Fig, 7, also
644 averaged over all radiosonde events, and show very similar correlations, RMSEs, and biases for
645 all PRs, implying that the impact of including RASS observations in the retrieval is minimal on
646 this variable. Finally, it is noted that Fig. 7 shows the mixing ratio of the data from TROPoe BC.
647 The radiosonde BC mixing ratio results are almost identical.

649
650
651
652
653
654

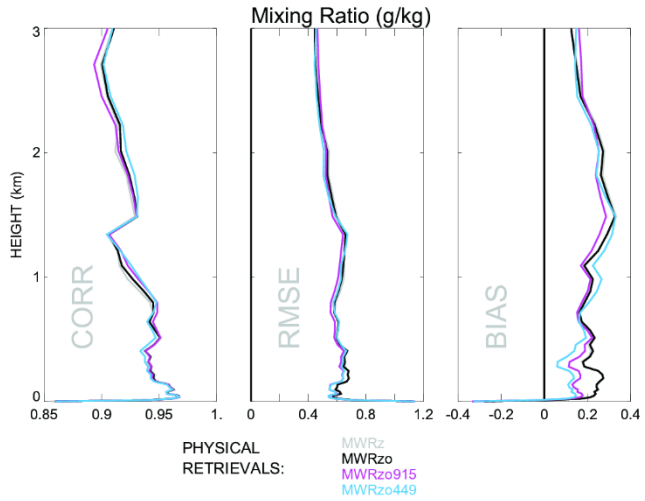

655 *Fig. 7. Same as the panels in Fig. 6b, but for mixing ratio, when using the TROPoe BC method on*
656 *the MWR Tbs.*
657

658 **4.2 Statistics for the profiles least close to the climatology**

659 Physical retrievals use climatological data as a constraint in the retrieval. Statistically,
660 the averaged profiles of both temperature and moisture variables are very close to the
661 climatological averages. However, the most interesting and difficult profiles to retrieve are the
662 cases furthest from climatology (Löhnert and Maier, 2012). To check the behavior of the
663 retrieved data in such "extreme" cases, the RMSE was first calculated for each radiosonde

profile relative to the prior profiles for 37 vertical levels from the surface up to 3 km AGL, and then the 15 cases with the largest 0-3 km layer averaged RMSEs compared to the prior were selected.

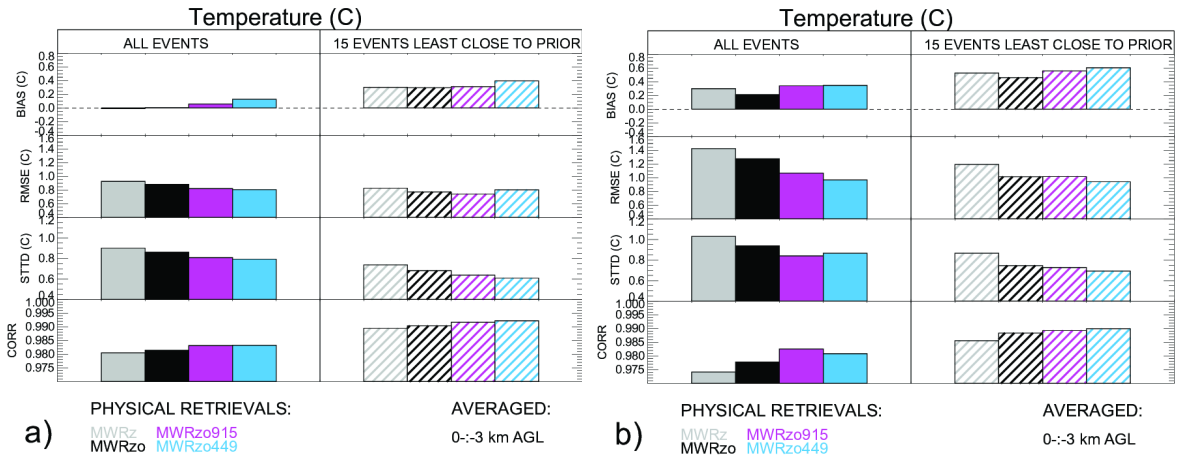

Fig. 8. From top to bottom: biases (retrievals minus radiosonde), RMSEs, standard deviations of the difference between retrievals and radiosonde, and Pearson correlations for the four PR configurations, averaged from the surface to 3 km AGL, and over all radiosonde data (solid boxes), and over the 15 extreme cases (hatched boxes). The data in panels a) use radiosonde BC, and in b) TROPoe BC on the MWR Tbs.

Figure 8 shows the temperature statistical analysis for the entire radiosonde data set (solid boxes) and for the fifteen events far from the climatological mean (hatched boxes) for bias, RMSE, standard deviation of the differences between retrievals and radiosonde data, and Pearson correlation, calculated as the weighted averaged over the 37 vertical heights up to 3 km AGL[1].

[1] The vertical grid used in the PRs is not uniform, with more frequent levels closer to the surface. If a simple average of the data from all levels is used, the near-surface layer will be weighted more compared to the upper levels of the retrievals. To avoid this, a vertical average over the lowest 3 km AGL is performed using weights at each vertical level determined by the distance between the levels.

677 Differences in the statistics when using the entire radiosonde data set or the fifteen
678 extreme profiles are noticeable for all statistical estimators. The PRs that include RASS
679 observations show better performance compared to the strictly MWR-only PR profiles (i.e.,
680 MWRz and MWRzo) for almost all statistical comparisons. This improvement is larger for the
681 PRs using the TROPoe BC (Fig. 8b) compared to the PRs using the radiosonde BC (Fig. 8a). Three
682 statistical estimators, RMSE, standard deviation, and Pearson correlation show overall better
683 values for the 15 extreme cases compared to the whole radiosonde dataset, for all PR
684 configurations and both BC approaches. This is due to the fact that for this dataset the monthly
685 averaged radiosonde profiles (for March and May particularly) depart quite substantially from
686 the monthly prior profiles. For example, the averaged radiosonde profile in March is warmer by
687 ~7 ^{o}C compared to the March prior (and in May by ~5 ^{o}C) in the first 3 km AGL. Consequently,
688 the extreme cases (mostly found in March) have the warmest radiosonde temperature profiles,
689 but are overall closer to the monthly averaged radiosonde profiles.
690 Table 2 includes the same data as in Figure 8 but as a percentage of the improvement,
691 compared to the MWRz retrievals.
692
693
694
695
696
697

0-3 km AGL	ALL EVENTS					15 EVENTS LEAST CLOSE TO THE PRIOR			
RADIOSONDE BIAS-CORRECTION									
	MWRz	MWRzo	MWRzo RASS915	MWRzo RASS449		MWRz	MWRzo	MWRzo RASS915	MWRzo RASS449
RMSE	0%	5%	11%	13%		0%	7%	10%	3%
STTD	0%	4%	10%	12%		0%	8%	14%	17%
CORR	0%	0.1%	0.3%	0.3%		0%	0.1%	0.2%	0.3%
TROPoe BIAS-CORRECTION									
RMSE	0%	10%	25%	32%		0%	15%	15%	21%
STTD	0%	9%	18%	16%		0%	14%	16%	20%
CORR	0%	0.4%	0.9%	0.7%		0%	0.3%	0.4%	0.4%

Table 2. Retrieval improvements for different RASS/MWR configurations as a percentage compared to MWRz.

The results presented in Table 2 show improvements in all statistical estimations when including RASS observations, with improvements in RMSE between 10 and 20 %, demonstrating the positive impact derived by the inclusion of the active measurements, regardless of the bias-correction method used, but larger for the TROPoe BC data because there is more room for improvement when this BC method is used. Improvements in the Pearson correlation

coefficients are small because correlation, determined during XPIA by the overall temperature structure with height and diurnal cycle, is already good, leaving little room for improvement.

4.3 Virtual temperature profile statistics

Using the physical retrieval outputs, “retrieved virtual temperature profiles” can also be calculated. In this section the direct comparison of these retrieved virtual temperature profiles and RASS virtual temperature profiles to the original radiosonde is shown. With this comparison we want to show how the biases of the retrieved profiles relate to the original RASS Tv biases.

Figure 9 shows Tv retrieved profile biases compared to the original radiosonde data. These Tv profiles and RASS 915 and RASS 449 Tv bias data are interpolated onto a regular vertical grid, going from 200 m to 1.6 km with a 100 m resolution, for easy comparison.

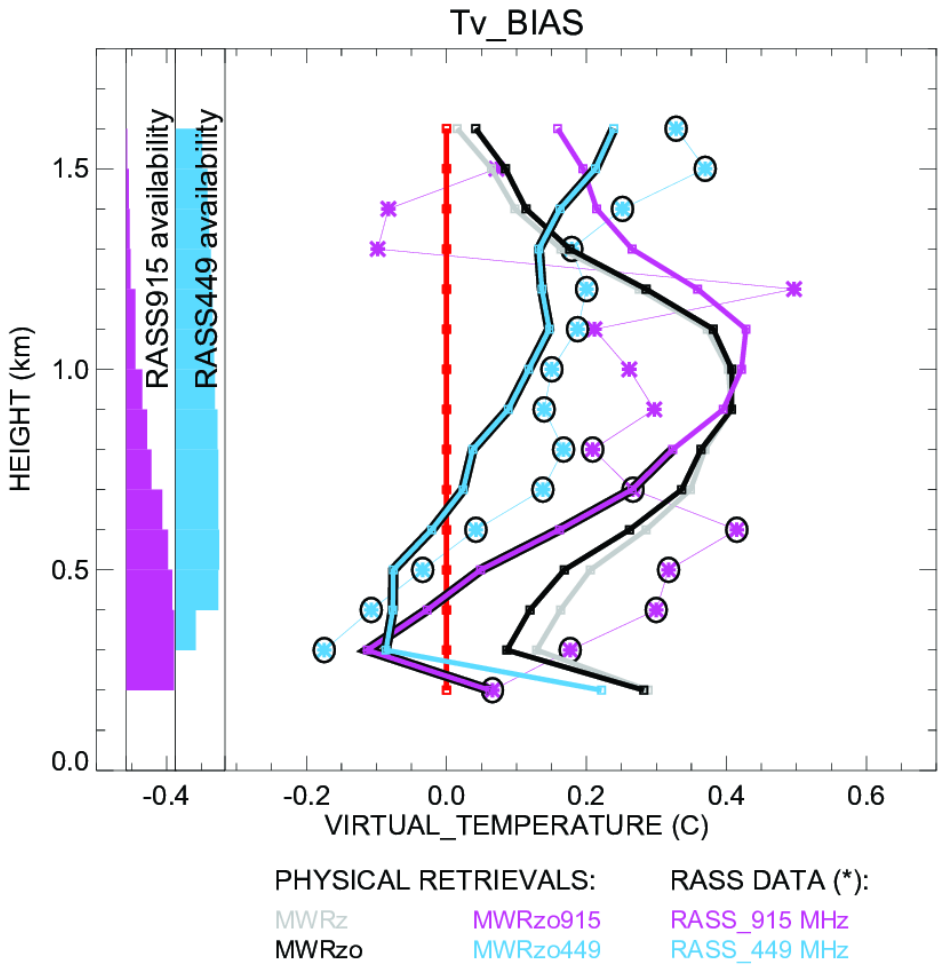

718

719 *Fig. 9. Bias of virtual temperature for all PR configurations compared to the original radiosonde*

720 *measurements. A zero bias is denoted by the red line. RASS data biases are marked by asterisks*

721 *and by additional circles for the RASS data with more than 50% availability, according to the*

722 *availability bar charts on the left.*

723 *All PRs profiles are derived after applying the radiosonde BC method.*

724

725 While RASS 449 data are available at almost all heights up to 1.6 km, the RASS 915 data

726 availability decreases considerably with height, lowering to 50% availability around 800 m AGL.

727 The PRs that include RASS data, MWRzo915 and MWRzo449, are also marked with additional
728 black lines at the heights with at least 50% of relative RASS data availability. In agreement with
729 Fig. 6a, this figure clearly shows the superiority of the MWRzo449 and MWRzo915 (in the layer
730 with > 50% RASS data availability) compared to the MWRz and MWRzo configurations, which
731 do not include RASS data. For MWRzo449, RASS 449 data were almost always available,
732 therefore it is easy to identify a similarity between the Tv bias profiles of the RASS 449 and the
733 PRs including it. Thus, for the MWRzo449 the Tv bias is more uniform through the heights
734 compared to all other PRs that do not include RASS data. Moreover, it is noted a roughly
735 constant offset between the MWRzo449 Tv and RASS 449 Tv biases profiles, with their
736 averaged difference equal to ~0.08 ^{o}C (when the radiosonde BC is used), and to ~0.32 ^{o}C (when
737 the TROPoe BC is used, not shown), over the ~1.3 km (0.3-1.6 km) atmospheric layer where
738 more than 50% of the RASS 449 measurements are available, uniformly distributed through the
739 heights. The inclusion of the RASS into the PRs does reduce the values of the biases in the
740 retrievals even below the values of the RASS biases, because of the combined information from
741 RASS and MWR.
742
743 **5. Conclusions**
744 In this study, data collected during the XPIA field campaign were used to test different
745 configurations of a physical-iterative retrieval (PR) approach in the determination of
746 temperature and humidity profiles from data collected by microwave radiometers, surface
747 sensors, and RASS measurements. The accuracy of several PR configurations was tested: two
748 configurations made use only of surface observations and MWR observed brightness

749 temperature (zenith only, MWRz; and zenith plus oblique, MWRzo); while two others included
750 the active virtual temperature profile observations available from co-located RASS (one, RASS
751 915, associated with a 915-MHz; and the other, RASS 449, associated with a 449-MHz wind
752 profiling radar). Radiosonde launches were used for verification of the retrieved profiles. In
753 Appendix A, the performance of MWRz and MWRzo retrieved profiles and Neural Network
754 retrieved profiles against the radiosondes was evaluated.

755 To remove any observational systematic error in the MWR Tb observations, two bias-
756 correction procedures were tested. The first one takes advantage of the many radiosondes
757 launched during XPIA, and the second one uses climatological profiles. As expected, the
758 radiosonde bias-correction method gives retrieved profiles closer to the radiosonde
759 temperature profiles than when using the climatological based method. Nevertheless, our
760 results show that regardless of the bias-correction method used, the inclusion of the
761 observations from the active RASS instruments in the PR approach improves the accuracy of the
762 temperature profiles by around 10-20% compared to the PR configuration using only surface
763 observations and MWR observed brightness temperature from the zenith scan. Of the PRs
764 configurations tested, generally better statistical agreement is found with the radiosonde
765 observations when the RASS 449 is used together with the surface observations and brightness
766 temperature from the zenith and averaged oblique MWR observations.

767 The **AKernel** and the posterior covariance matrices for temperature are used to derive
768 the one-sigma uncertainty, vertical resolution, and cumulative degree of freedom as a function
769 of height for the different PRs, and the level-to-level correlated uncertainty of the retrievals.
770 Results show that the inclusion of the active instruments improves all of the above-mentioned

771 variables in the 0-3km layer, including at heights between 2-3km that are above the maximum
772 RASS height. Thus, the positive impact of the RASS observations extends into the atmosphere
773 above the height of measurements themselves.

774 Furthermore, 15 cases when temperature profiles from the radiosonde observations
775 were the furthest away from the mean climatological average were selected, and the statistical
776 comparison was reproduced over this subset of cases. These are the cases usually the most
777 difficult to retrieve and the most important to forecast; therefore, it is essential to improve the
778 retrievals in these situations. Even for this subset of selected cases the inclusion of active
779 sensor observations in the PRs is found to be beneficial.

780 Finally, the impact of the inclusion of RASS measurements on the retrieved humidity
781 profiles was considered, but the inclusion of RASS observations did not produce significantly
782 better results, compared to the configurations that do not include them. This was not a surprise
783 as RASS measures virtual temperature, effectively adding very little extra information to the
784 water vapor retrieval. In this case a better option would be to consider adding other active
785 remote sensors such as water vapor differential absorption lidars (DIALs) to the PRs. Turner and
786 Löhnert (2021) showed that including the partial profile of water vapor observed by the DIAL
787 substantially increases the information content in the combined water vapor retrievals.
788 Consequently, to improve both temperature and humidity retrievals a synergy between MWR,
789 RASS, and DIAL systems would likely be necessary.

790

791 **Appendix A**

792 The neural network (NN) retrievals developed by the vendor explicitly for XPIA use a
793 training dataset based on a 5-year climatology of profiles from radiosondes launched at the
794 Denver International Airport, 35 miles south-east from the XPIA site. NN-based MWR vertical
795 retrieval profiles were obtained using the zenith or an average of two oblique elevation scans,
796 15- and 165-degrees (not including the zenith), all with 58 levels extending from the surface up
797 to 10 km, with nominal vertical grid depending on the height (every 50 m from the surface to
798 500 m, every 100 m from 500 m to 2 km, and every 250 m from 2 to 10 km, AGL).
799 Fig. 1A shows composite NN vertical profiles of temperature (separately for the zenith
800 and averaged obliques) calculated for radiosonde launch times, and the corresponding PR
801 profiles already introduced in Fig. 6a, b. For a proper comparison, only MWRz and MWRzo
802 profiles are used, without including RASS measurements. It has to be noted that since the "NN
803 oblique" retrieval provided by the manufacturer of the radiometer does not include the zenith,
804 this configuration cannot be considered exactly equivalent to the MWRzo PR.

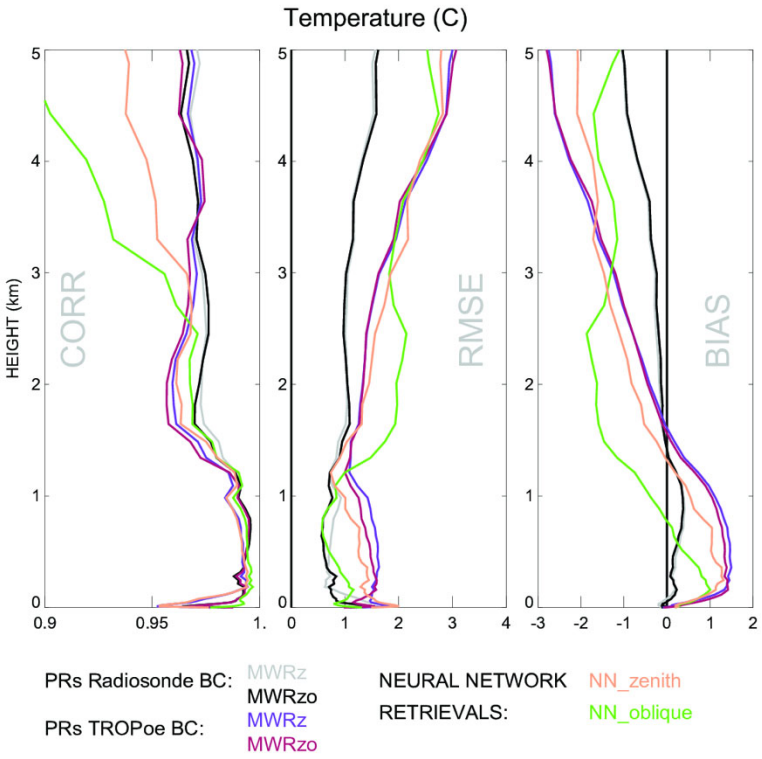

Fig. 1A. Pearson correlation, RMSE, and mean bias for temperature profiles for MWRz in grey (and purple) and MWRzo in black (and maroon) when the radiosonde BC (and the TROPoe BC) method is applied. Included in this figure are the NN temperature profiles, from the zenith scan (in beige), and from the averaged oblique scans (in green).

Another difference to point out is that, while the MWR Tb data have been bias-corrected before being used in the PR configurations, as discussed in Section 3.2, the NN retrievals use the uncorrected Tb, since it was non-trivial to reprocess those retrievals. Martinet et al. (2015) showed that when it is possible to bias-correct the MWR Tb before applying the NN retrieval technique, the NN retrievals are not impacted below 1 km AGL, but a clear improvement of NN retrievals in terms of RMSE and bias are observed between 1 and 3 km

827 altitude. As is visible in Fig. 1A, this is the layer of the atmosphere where the NN profiles (beige
828 and green lines) have larger bias and RMSE, compared to the PR profiles.

829 When the radiosonde BC method is used, the MWRz and MWRzo PRs (gray and black
830 lines) present better statistics through the entire profiles shown in Fig. 1A, with larger values of
831 the correlation coefficient, and smaller values of RMSE and bias. The oblique only NN profiles
832 (in green) show comparable statistics to the PRs employing the radiosonde BC method up to 1
833 km AGL, with degraded performances above this height. Above 1 km AGL, the zenith NN
834 profiles (in beige) do better than the oblique NN in terms of RMSE and bias. When the TROPoe
835 BC method is used, the MWRz and MWRzo PRs (purple and maroon lines) perform better than
836 the NN profiles only in terms of RMSE and bias, and only between 1.5 and 3 km AGL.

837 The better performance obtained by the MWRz and MWRzo PRs that use the
838 radiosonde BC approach demonstrate the importance of having an accurate and reliable
839 method for bias correcting the MWR.

840

841 **Data availability**

842 All data are publicly accessible at the DOE Atmosphere to Electrons Data Archive and
843 Portal, found at https://a2e.energy.gov/projects/xpia (Lundquist et al., 2016).

844

845 **Author contribution**

846 Irina Djalalova completed the primary analysis using the XPIA dataset. Daniel Gottas
847 contributed to the post-processing of the RASS data. Dave Turner modified the TROPoe

algorithm to include the RASS data as input. All authors contributed to the analysis of the results. Irina Djalalova prepared the manuscript with contributions from all co-authors.

Acknowledgements

We thank all the people involved in XPIA for instrument deployment and maintenance, data collection, and data quality control, and particularly the University of Colorado Boulder for making the CU MWR data available. We are very grateful for the constructive comments and suggestions provided by the two anonymous Referees and by the Editor, which we believe have greatly improved the clarity of the manuscript. Funding for this study was provided by the NOAA/ESRL Atmospheric Science for Renewable Energy (ASRE) program.

Competing interests

The authors declare no competing interests.

References

Adachi, A. and H. Hashiguchi: Application of parametric speakers to radio acoustic sounding system. **ATMOS MEAS TECH**, **12**, 5699–5715, https://doi.org/10.5194/amt-12-5699-2019, 2019.

Adler, B., J. M. Wilczak, L. Bianco, I. Djalalova, J. B. Duncan Jr., D. D. Turner: Observational case study of a persistent cold air pool and gap flow in the Columbia River Basin. **J APPL METEOROL CLIM**, 60, 1071-1090, https://doi.org/10.1175/JAMC-D-21-0013.1, 2021.

869 Banta, R. M., and coauthors: Characterizing NWP model errors using Doppler lidar
870 measurements of recurrent regional diurnal flows: Marine-air intrusions into the
871 Columbia River Basin. **MON WEATHER REV**, **148**, 927-953,
872 https://doi.org/10.1175/MWR-D-19-0188.1, 2020.
873 Bianco L., D. Cimini, F. S. Marzano, and R. Ware: Combining microwave radiometer and wind
874 profiler radar measurements for high-resolution atmospheric humidity profiling, **J**
875 **ATMOS OCEAN TECH**, **22**, 949–965, https://doi.org/10.1175/JTECH1771.1, 2005.
876 Bianco, L., K. Friedrich, J. M. Wilczak, D. Hazen, D. Wolfe, R. Delgado, S. Oncley, and J. K.
877 Lundquist: Assessing the accuracy of microwave radiometers and radio acoustic
878 sounding systems for wind energy applications. **ATMOS MEAS TECH**, **10**, 1707-1721,
879 https://doi.org/10.5194/amt-10-1707-2017, 2017.
880 Cadeddu, M. P., J. C. Liljegren, and D. D. Turner: The Atmospheric radiation measurement
881 (ARM) program network of microwave radiometers: instrumentation, data, and
882 retrievals, **ATMOS MEAS TECH**, **6**, 2359–2372, https://doi.org/10.5194/amt-6-2359-
883 2013, 2013.
884 Cimini, D., T. J. Hewison, L. Martin, J. Guldner, C. Gaffard, F. S. Marzano: Temperature and
885 humidity profile retrievals from ground-based microwave radiometers during TUC,
886 **METEOROL Z**, Vol. 15, No. 5, 45-56, DOI: 10.1127/09411-D-2948/2006/0099, 2006.
887 Cimini, D., E. Campos, R. Ware, S. Albers, G. Giuliani, J. Oreamuno, P. Joe, S. E. Koch, S. Cober,
888 and E. Westwater: Thermodynamic Atmospheric Profiling during the 2010 Winter
889 Olympics Using Ground-based Microwave Radiometry, **IEEE T GEOSCI REMOTE**, **49**, 12,
890 https://doi.org/10.1109/TGRS.2011.2154337, 2011.

891 Cimini, D., Rosenkranz, P. W., Tretyakov, M. Y., Koshelev, M. A., and Romano, F.: Uncertainty of
892 atmospheric microwave absorption model: impact on ground-based radiometer
893 simulations and retrievals, **ATMOS CHEM PHYS**, **18**, 15231–15259,
894 https://acp.copernicus.org/articles/18/15231/2018, 2018.
895 Cimini, D., M. Haeffelin, S. Kotthaus, U. Löhnert, P. Martinet, E. O'Connor, C. Walden, M.
896 Collaud Coen, and J. Preissler: Towards the profiling of the atmospheric boundary layer
897 at European scale—introducing the COST Action PROBE. **Bulletin of Atmospheric**
898 **Science and Technology**, **1**, 23–42, https://doi.org/10.1007/s42865-020-00003-8, 2020.
899 Clough, S.A., M. W. Shephard, E. J. Mlawer, J. S. Delamere, M. Iacono, K. E. Cady-Pereira, S.
900 Boukabara and P. D. Brown: Atmospheric radiative transfer modeling: A summary of the
901 AER codes, **J QUANT SPECTROSC RA**, vol 91, no. 2, pp 233-244,
902 https://doi.org/10.1016/j.jqsrt.2004.05.058, 2005.
903 Crewell, S., U. Löhnert: Accuracy of Boundary Layer Temperature Profiles Retrieved With
904 Multifrequency Multiangle Microwave Radiometry, **IEEE T GEOSCI REMOTE**, VOL. 45,
905 NO. 7, JULY 2007, DOI: 10.1109/TGRS.2006.888434, 2007.
906 Engelbart, D., W. Monna, J. Nash: Integrated Ground-Based Remote-Sensing Stations for
907 Atmospheric Profiling, **COST Action 720 Final Report**, EUR 24172,
908 https://doi.org/10.2831/10752, 2009.
909 Görsdorf, U., and V. Lehmann: Enhanced Accuracy of RASS-Measured Temperatures Due to an
910 Improved Range Correction. **J ATMOS OCEAN TECH**, **17 (4)**, 406–416,
911 https://doi.org/10.1175/1520-0426(2000)017<0406:EAORMT>2.0.CO;2, 2000.

912 Han, Y., and E. R. Westwater: Remote sensing of tropospheric water vapor and cloud liquid
913 water by integrated ground-based sensors. **J ATMOS OCEAN TECH**, **12**, 1050-1059, DOI:
914 https://doi.org/10.1175/1520-0426(1995)012<1050:RSOTWV>2.0.CO;2, 1995.
915 Hewison, T.: 1D-VAR Retrieval of Temperature and Humidity Profiles From a Ground-Based
916 Microwave Radiometer, **IEEE T GEOSCI REMOTE**, **45(7)**, 2163–2168,
917 https://doi.org/10.1109/TGRS.2007.898091, 2007.
918 Horst, T. W., S. R. Semmer, and I. Bogoev: Evaluation of Mechanically-Aspirated
919 Temperature/Relative Humidity Radiation Shields, 18th Symposium on Meteorological
920 Observation and Instrumentation, AMS Annual Meeting, New Orleans, LA, 10-15
921 January 2016, https://ams.confex.com/ams/96Annual/webprogram/Paper286839.html,
922 2016.
923 Kaimal, J. C., and J. E. Gaynor: The Boulder Atmospheric Observatory. **J CLIM APPL METEOROL**,
924 **22**, 863–880, https://doi.org/10.1175/1520-0450(1983)022<0863:TBAO>2.0.CO;2, 1983.
925 Küchler, N., D. D. Turner, U. Löhnert,and S. Crewell: Calibrating ground-based microwave
926 radiometers: Uncertainty and drifts, **RADIO SCI**, **51**, 311–327,
927 doi:10.1002/2015RS005826, 2016.
928 Löhnert U. and O. Maier: Operational profiling of temperature using ground-based microwave
929 radiometry at Payerne: prospects and challenges. **ATMOS MEAS TECH**, **5**, 1121–1134,
930 https://doi.org/10.5194/amt-5-1121-2012, 2012.
931 Lundquist, J. K., J. M. Wilczak, R. Ashton, L. Bianco, W. A. Brewer, A. Choukulkar, A. Clifton, M.
932 Debnath, R. Delgado, K. Friedrich, S. Gunter, A. Hamidi, G. V. Iungo, A. Kaushik, B.
933 Kosović, P. Langan, A. Lass, E. Lavin, J. C.-Y. Lee, K. L. McCaffrey, R. K. Newsom, D. C.

Noone, S. P. Oncley, P. T. Quelet, S. P. Sandberg, J. L. Schroeder, W. J. Shaw, L. Sparling, C. St. Martin, A. St. Pe, E. Strobach, K. Tay, B. J. Vanderwende, A. Weickmann, D. Wolfe, and R. Worsnop: Assessing state-of-the-art capabilities for probing the atmospheric boundary layer: the XPIA field campaign. **B AM METEOROL SOC**, **98**, 289–314, https://doi.org/10.1175/BAMS-D-15-00151.1, 2017.

Maahn, M., D. D. Turner, U. Löhnert, D. J. Posselt, K. Ebell, G. G. Mace, and J. M. Comstock: Optimal estimation retrievals and their uncertainties: What every atmospheric scientist should know. **B AM METEOROL SOC**, **101**, E1512-E1523, https://doi.org/10.1175/BAMS-D-19-0027.1, 2020.

Maddy, E. S. and C. D. Barnet: Vertical Resolution Estimates in Version 5 of AIRS Operational Retrievals. **IEEE T GEOSCI REMOTE**, VOL. **46**, NO. 8, AUGUST 2008, https://doi.org/10.1109/TGRS.2008.917498, 2008.

Martinet, P., A. Dabas, J.-M. Donier, T. Douffet, O. Garrouste, and R. Guillot: 1D-Var temperature retrievals from microwave radiometer and convective scale model, **TELLUS A**, **67:1**, https://doi.org/10.3402/tellusa.v67.27925, 2015.

Martinet, P., D. Cimini, F. Burnet, B. Ménétrier, Y. Michel, and V. Unger: Improvement of numerical weather prediction model analysis during fog conditions through the assimilation of ground-based microwave radiometer observations: a 1D-Var study, **ATMOS MEAS TECH**, **13**, 6593–6611, https://doi.org/10.5194/amt-13-6593-2020, 2020.

May, P. T. and J. M. Wilczak: Diurnal and Seasonal Variations of Boundary-Layer Structure Observed with a Radar Wind Profiler and RASS. **MON WEATHER REV**, **121**, 673–682, https://doi.org/10.1175/1520-0493(1993)121<0673:DASVOB>2.0.CO;2, 1993.

Masiello, G., C. Serio, and P. Antonelli: Inversion for atmospheric thermodynamical parameters of IASI data in the principal components space. **Q J ROY METEOR SOC**, **138**, 103–117, https://doi.org/10.1002/qj.909, 2012.

Merrelli, A. M., and D. D. Turner: Comparing information content of upwelling far infrared and midinfrared radiance spectra for clear atmosphere profiling. **J ATMOS OCEAN TECH**, **29**, 510–526, https://doi.org/10.1175/JTECH-D-11-00113.1, 2012.

Neiman, P. J., D. J. Gottas, and A. B. White: A Two-Cool-Season Wind Profiler–Based Analysis of Westward-Directed Gap Flow through the Columbia River Gorge. **MON WEATHER REV**, **147**, 4653-4680, https://doi.org/10.1175/MWR-D-19-0026.1, 2019.

North, E. M., A. M.Peterson, and H. D. Parry: RASS, a remote sensing system for measuring low-level temperature profiles. **B AM METEOROL SOC**, **54**, 912–919, 1973.

Payne, V. H., J. S. Delamere, K. E. Cady-Pereira, R. R. Gamache, J.-L. Moncet, E. J. Mlawer, and S. A. Clough: Air-broadened half-widths of the 22- and 183-GHz water-vapor lines. **IEEE T GEOSCI REMOTE**, **46**, 3601-3617, https://doi.org/10.1109/TGRS.2008.2002435, 2008.

Payne, V. H., E. J. Mlawer, K. E. Cady-Pereira, and J.-L. Moncet: Water vapor continuum absorption in the microwave. **IEEE T GEOSCI REMOTE**, **49**, 2194-2208, https://doi.org/10.1109/TGRS.2010.2091416, 2011.

Rodgers, C. D.: Inverse Methods for Atmospheric Sounding: Theory and Practice. Series on Atmospheric, Oceanic and Planetary Physics, Vol. 2, World Scientific, 238 pp, 2000.

Rosenkranz, P. W.: Water vapour microwave continuum absorption: A comparison of measurements and models. **RADIO SCI**, **33**, 919–928, https://doi.org/10.1029/98RS01182, 1998.

978 Shaw, W., and Coauthors: The Second Wind Forecast Improvement Project (WFIP 2): General
979 Overview. **B AM METEOROL SOC**, **100(9)**, 1687–1699, https://doi.org/10.1175/BAMS-D-
980 18-0036.1, 2019.
981 Solheim, F., J. R. Godwin, J., and R. Ware: Passive ground-based remote sensing of atmospheric
982 temperature, water vapor, and cloud liquid profiles by a frequency synthesized
983 microwave radiometer. **METEOROL Z**, **7**, 370–376, 1998a.
984 Solheim F., J. R. Godwin, E. R. Westwater, Y. Han, S. J. Keihm, K. Marsh, R. Ware: Radiometric
985 profiling of temperature, water vapor and cloud liquid water using various inversion
986 methods. **RADIO SCI**, **33**, 393–404, https://doi.org/10.1029/97RS03656, 1998b.
987 Stankov, B. B., E. R. Westwater, and E. E. Gossard: Use of wind profiler estimates of significant
988 moisture gradients to improve humidity profile retrieval. **J ATMOS OCEAN TECH**, **13**,
989 1285-1290, DOI:
990 https://doi.org/10.1175/15200426(1996)013<1285:UOWPEO>2.0.CO;2, 1996.
991 Strauch, R. G., D. A. Merritt, K. P. Moran, K. B. Earnshaw, and D. V. De Kamp: The Colorado
992 wind-profiling network. **J ATMOS OCEAN TECH**, **1**, 37–49, https://doi.org/10.1175/1520-
993 0426(1984)001<0037:tcwpn>2.0.co;2, 1984.
994 Turner, D. D.: Improved ground-based liquid water path retrievals using a combined infrared
995 and microwave approach. **J GEOPHYS RES-ATMOS, 112**, D15204,
996 https://doi.org/10.1029/2007JD008530, 2007.
997 Turner, D. D., and U. Löhnert: Information content and uncertainties in thermodynamic profiles
998 and liquid cloud properties retrieved from the ground-based Atmospheric Emitted

Radiance Interferometer (AERI). **J APPL METEOROL CLIM**, **53**, 752–771, https://doi.org/10.1175/JAMC-D-13-0126.1, 2014.

Turner, D. D., and W. G. Blumberg: Improvements to the AERIoe thermodynamic profile retrieval algorithm. **IEEE J-STARS**, **12(5)**, 1339–1354, https://doi.org/10.1109/JSTARS.2018.2874968, 2019.

Turner, D. D., and U. Löhnert: Ground-based Temperature and Humidity Profiling: Combining Active and Passive Remote Sensors. **ATMOS MEAS TECH**, **14**, 3033–3048, https://doi.org/10.5194/amt-2020-352, 2021.

Ware R., Solheim F., Carpenter R., and Coauthors: A multi-channel radiometric profiler of temperature, humidity and cloud liquid. **RADIO SCI**, **38**, No. 4, 8079, https://doi.org/10.1029/2002RS002856, 2003.

Weber, B. L., D. B. Wuertz, D. C. Welsh, and R. Mcpeek: Quality controls for profiler measurements of winds and RASS temperatures. **J ATMOS OCEAN TECH**, **10**, 452–464, https://doi.org/10.1175/1520-0426(1993)010<0452:qcfpmo>2.0.co;2, 1993.

Wilczak, J. M., and Coauthors: The Second Wind Forecast Improvement Project (WFIP2): Observational Field Campaign. **B AM METEOROL SOC**, **100(9)**, 1701–1723, https://doi.org/10.1175/BAMS-D-18-0035.1, 2019.

Wolfe, D. E. and R. J. Lataitis: Boulder Atmospheric Observatory: 1977–2016: The end of an era and lessons learned. **B AM METEOROL SOC**, **99**, 1345–1358, https://doi.org/10.1175/BAMS-D-17-0054.1, 2018.